

Application of the Turbulent Potential Model to Unsteady Flows and Three-Dimensional Boundary Layers

J. Blair Perot, Sasanka Are, and Xing Zhang

Department of Mechanical and Industrial Engineering, University of Massachusetts, Amherst, Amherst, Massachusetts, USA

The turbulent potential model is a Reynolds-averaged (RANS) turbulence model that is theoretically capable of capturing nonequilibrium turbulent flows at a computational cost and complexity comparable to two-equation models. The ability of the turbulent potential model to predict nonequilibrium turbulent flows accurately is evaluated in this work. The flow in a spanwise-driven channel flow and over a swept bump are used to evaluate the turbulent potential model's ability to predict complex three-dimensional boundary layers. Results of turbulent vortex shedding behind a triangular and a square cylinder are also presented in order to evaluate the model's ability to predict unsteady flows. Early indications suggest that models of this type may be capable of significantly enhancing current numerical predictions of turbomachinery components at little extra computational cost or additional code complexity.

Keywords Modeling, Three-dimensional, Turbulence, Unsteady

Three-dimensional boundary layers and unsteady vortex shedding represent situations that are common in many engineering flows. These flow situations are examples in which the turbulence does not have time to reach equilibrium with the mean flow. Flows on aircraft wings, inside curved ducts or bends on rotating disks and propellers, and at junctions of stationary walls of fluid machinery are good examples of nonequilibrium flows.

Previous research has indicated that two-equation models, which assume that the Reynolds-stress tensor is aligned with

the velocity-gradient tensor, are not accurate for nonequilibrium flows. When such models were applied to three-dimensional shear-driven or pressure-driven flows (nonequilibrium flows), they yielded poor results (Bradshaw et al., 1996; Fannelop et al., 1975). Ölçmen and Simpson (1993) reviewed the performance of more complicated algebraic (or nonlinear) eddy-viscosity models and concluded that none of the models could perform well in all the cases studied. The models that accounted for the anisotropy of the eddy viscosity performed better in general. However, the anisotropic constants had to be changed for different flows.

Reynolds stress transport models can predict nonequilibrium flows because they do not hypothesize a constitutive relationship between the Reynolds stress and mean flow gradients. However, the Reynolds stress transport models tend to be more expensive and numerically stiff. Durbin (1993a) proposed an elliptical Reynolds stress model that could reproduce some of the features observed by Moin and colleagues (1990) in a three-dimensional channel flow. For the unsteady vortex shedding behind a bluff body, Franke and Rodi (1991) compared the ability of different models to predict turbulent vortex shedding from a rectangular cylinder. Their conclusion is that some κ - ϵ models do not predict the right shedding frequency, but more expensive Reynolds stress transport models can produce results that are in good agreement with the experiments.

The turbulent potential model should be able to capture nonequilibrium situations at a cost comparable to that of two-equation models. The model does not hypothesize an explicit relationship between the turbulence and the mean flow and it is the least expensive RANS model that is theoretically capable of capturing nonequilibrium turbulent flows. Nonequilibrium occurs when the mean flow changes rapidly in time or in space along the flow direction more quickly than the turbulence can respond. Turbulent nonequilibrium is a persistent characteristic of large-scale unsteady flows such as bluff body vortex shedding and of accelerated flows such as three-dimensional boundary layers. Detailed information on the development and formulation

Received 25 June 2002; accepted 1 July 2002.

We gratefully acknowledge the support of the Office of Naval Research, grant N00014-99-0194.

Address correspondence to J. Blair Perot, Department of Mechanical and Industrial Engineering, University of Massachusetts, Amherst, Amherst, MA 01003, USA. E-mail: perot@ecs.umass.edu

of the turbulent potential model can be found in Perot (1999) and Perot and Wang (1999). The particular emphasis in this work is evaluating and enhancing the model's performance in three-dimensional boundary layers and unsteady flows.

TURBULENT POTENTIAL MODEL

The transport equations that constitute the turbulent potential model are summarized as follows:

$$\begin{aligned} \frac{Dk}{Dt} &= \nabla \cdot (v + v_t \bar{\sigma}_k) \nabla k + P - \varepsilon \\ \frac{D\varepsilon}{Dt} &= \nabla \cdot (v + v_t \bar{\sigma}_\varepsilon) \nabla \varepsilon + \frac{\hat{\varepsilon}}{k} (C_{\varepsilon 1} P - C_{\varepsilon 2} \varepsilon + C_{\varepsilon 3} P_{3D}) \\ \frac{D(\phi/k)^{1/2}}{Dt} &= \nabla \cdot (v + v_t \bar{\sigma}_k) \nabla (\phi/k)^{1/2} \\ &\quad - \frac{1}{2} (1 - C_{p2}) \left(\frac{\phi}{k} \right)^{1/2} \frac{P}{k} \\ &\quad + \frac{1}{2} C_{p1} \frac{v_t}{v_t + 10\nu} \frac{\hat{\varepsilon}}{k} (2\alpha - 1) \left(\frac{\phi}{k} \right)^{1/2} \\ \frac{D(\psi/k)}{Dt} &= \nabla \cdot (v + v_t) \nabla (\psi/k) + 0.21 (2\alpha - 1) \frac{\phi}{k} \omega \\ &\quad - C_{p3} 2\alpha \frac{\psi}{k} P - C_{p1} \frac{v_t}{v_t + 10\nu} \frac{\hat{\varepsilon}}{k} (1 - \alpha) \frac{\psi}{k} \\ &\quad - (1 - C_{p2}) \left(\frac{\psi}{k} \frac{P}{k} - \frac{\phi}{k} \omega \right) \end{aligned}$$

where ϕ and ψ are the scalar and vector potentials, respectively.

$$\begin{aligned} P &= \psi \cdot \omega, \quad P_{3D} = |\psi \times \omega|, \quad v_t = C_\mu \frac{\phi k}{\varepsilon} \\ \alpha &= \left(1 + 1.5 \frac{\phi}{k} \right)^{-1} \\ \hat{\varepsilon} &= \varepsilon / (1 + 10\nu \nabla \sqrt{k}/k) \end{aligned}$$

Constants are:

$$\begin{aligned} C_\mu &= 0.21, \quad C_{p1} = 1.7, \quad C_{p2} = \frac{3}{5}, \quad C_{p3} = 0.12 \\ C_{\varepsilon 1} &= 1.45, \quad C_{\varepsilon 2} = 1.83 - 0.16 \exp \left(-0.1 \frac{k^2}{\nu \varepsilon} \right) \\ C_{\varepsilon 3} &= 0.15; \quad \text{and} \\ \bar{\sigma}_k &= 0.33 + 0.67 P/\hat{\varepsilon}, \quad \bar{\sigma}_\varepsilon = 0.33 + 0.5 P/\hat{\varepsilon} \end{aligned}$$

NUMERICAL METHOD

The numerical method uses an unstructured staggered mesh scheme that can conserve mass, momentum, and kinetic energy to machine precision. The turbulence quantities are advected using an upwinding scheme to guarantee positivity constraints. The model integrates up to the wall, so wall functions are not used, but the first grid point should be in the laminar sublayer to obtain accurate predictions. The details of this numerical method,

including accuracy analysis and conservation properties are discussed in Perot (2000) and Perot and Zhang (1999).

THREE-DIMENSIONAL BOUNDARY LAYERS

The turbulent body force potential model's ability to predict three-dimensional boundary layers is studied using two different three-dimensional boundary layers. The first was a spanwise-driven channel flow. In this flow, a large spanwise pressure gradient is suddenly applied to a fully developed channel flow. The pressure gradient produces a horizontally homogeneous flow (Figure 1) that develops in time. The mean velocity vector skews with height as the flow turns most quickly near the wall. Spanwise-driven channel flow at a bulk velocity Reynolds number of 3300 was simulated by Moin and colleagues (1990) using direct numerical simulation (DNS). Durbin (1993a) also modeled this flow with a Reynolds stress transport model. A two-equation RANS model would not be expected to produce good results for this flow because the turbulence effects would appear instantly in the spanwise direction rather than taking some time to develop. The turbulent potential model predictions of the turbulence quantities are improved by adding an extra production term to the dissipation evolution equation. We add a term $|\psi \times \omega|$ where ω is the mean vorticity and ψ is the turbulent potential. This term is zero in two-dimensional problems and has some similarities with the classic production term $\psi \cdot \omega$. This extra term captures the breakup of turbulent structures due to three-dimensional acceleration and the resulting drop in turbulence intensities.

The DNS data is for a channel flow where the suddenly applied spanwise pressure gradient is 10 times the streamwise pressure gradient. The data are given at the time of the spanwise pressure gradient application ($t = 0$) and at time increments of 0.3 thereafter up to a nondimensional time of 0.9. All quantities are nondimensionalized by the channel half-width and the initial shear velocity. The dimensionless viscosity is $0.00556 = 1/180$. The spanwise velocity increases rapidly during this time and reaches the same order of magnitude as the streamwise velocity. The turbulence cannot be considered to be in equilibrium at any time during this simulation because the eddy turnover time is of the order of one. Curiously, in this flow, the turbulent intensities decrease initially. This is counterintuitive, as one would expect

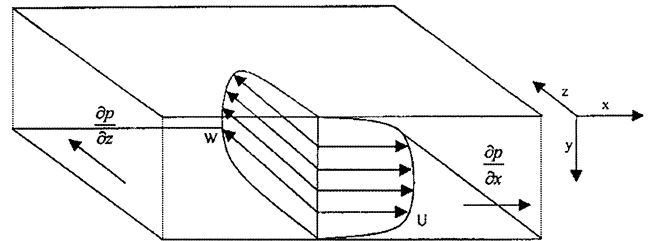


FIGURE 1

Schematic of a two-dimensional channel flow subjected to a spanwise pressure gradient.

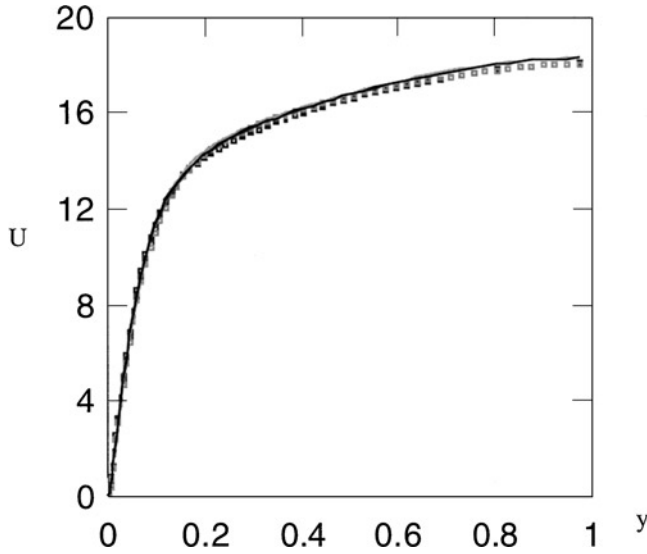


FIGURE 2

Streamwise mean velocity at times of 0.0, 0.3, 0.6, and 0.9. The symbols are DNS data (Moin et al., 1990); the solid lines are the turbulent potential model predictions.

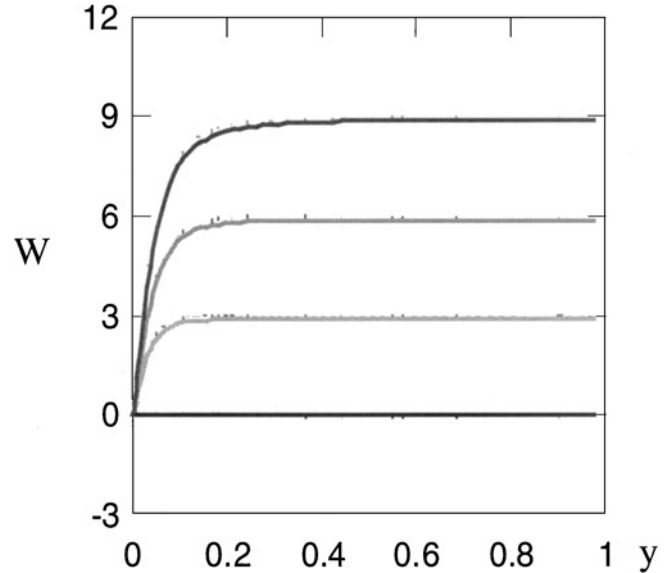


FIGURE 3

Spanwise mean velocity at times of 0.0, 0.3, 0.6, and 0.9. The symbols are DNS data (Moin et al., 1990); the solid lines are the turbulent potential model predictions.

an increase in the turbulent intensity because of the increase in magnitude of the shear due to the additional pressure gradient.

The mean streamwise velocity is shown in Figure 2. The symbols are the DNS data and the solid lines are the model predictions. This convention remains the same in all future graphs involving the spanwise-driven channel flow. It is seen clearly that in both the DNS data and the model predictions, there is not any significant change in the streamwise velocity during the initial development of the flow.

The mean spanwise velocity is shown in Figure 3. The mean spanwise velocity is roughly half the mean streamwise velocity at the final measurement time. The agreement with the DNS data is good. Visual comparison with the fully turbulent streamwise velocity profile makes it clear that the spanwise velocity boundary layer is essentially laminar at these early times. The turbulence may just have begun to affect the spanwise velocity at the final time. The standard k/ε and other models, which assume equilibrium, would have applied the full turbulent-eddy viscosity to the spanwise velocity and thereby have caused the spanwise boundary layer to grow much more rapidly as a turbulent boundary layer. Since the turbulence potential model is nonequilibrium in nature, the spanwise velocity predictions of the model are in good agreement with the DNS data.

In flows with a single inhomogeneous direction, such as spanwise-driven channel flow, there is a direct correspondence between the turbulent potentials and some of the Reynolds stresses, which allows a direct comparison to take place. In the more complex flows (shown later), comparison with the turbulence quantities is theoretically possible but highly impractical. The $\overline{u'v'}$ and $\overline{v'w'}$ shear stresses are shown in Figure 4. The upper set of curves are the $\overline{u'v'}$ shear stresses, and those stresses

directly influence the evolution of the streamwise velocity. The curves actually proceed from top to bottom as $t = 0.0, 0.3, 0.9, 0.6$, showing that this stress initially drops very slowly; between $t = 0.3$ and $t = 0.6$ it drops much more rapidly, and then after that it begins to increase toward its initial value. The model predictions decrease monotonically but display similar

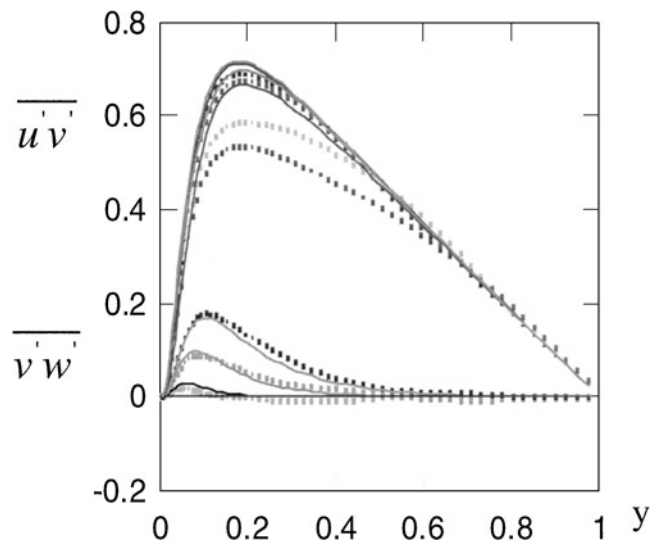


FIGURE 4

Turbulent shear stress profiles at 0.0, 0.3, 0.6, and 0.9. The symbols are DNS data (Moin et al., 1990); the solid lines are the turbulent potential model predictions. The upper group of curves are $\overline{u'v'}$, and the lower group of curves are $\overline{v'w'}$.

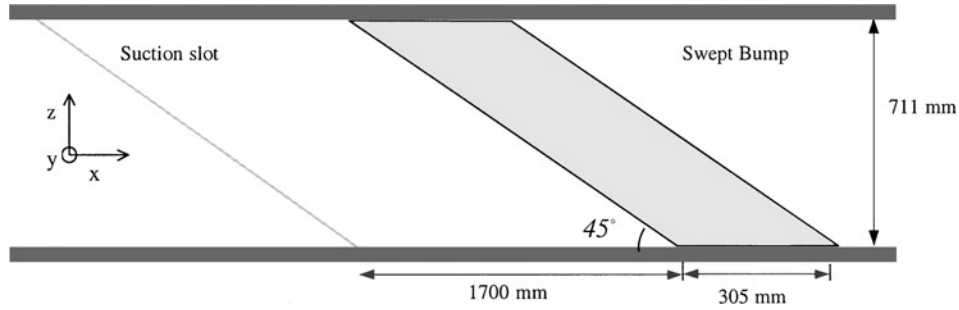


FIGURE 5

Top view of the swept bump.

qualitative behavior. The initial drop is very small but speeds up at later times. If the calculation is allowed to proceed past $t = 0.9$, the stress begins to increase, as with the DNS data. Although the predictions do not match exactly, the discrepancy appears to be a simple time lag in the predictions because the model predictions at $t = 1.2$ (not shown) are close to DNS data at $t = 0.9$. The mean flow predictions for the streamwise velocity show that, at least at these early times, the time-lag defect is not fundamentally important in predicting the mean flow.

The lower group of curves in Figure 4 are for the shear stress. The DNS data show that this stress starts at zero and then increases monotonically as time proceeds. After a long time, this stress can be expected to be 10 times larger than the $\overline{u'v'}$ shear stress. However, at these early times it is relatively small. The model predictions closely match the DNS data at these early times. The small magnitude of this stress at early times leads to the essentially laminar velocity profile for spanwise mean velocity.

While the turbulent potential model predicts the spanwise shear stress well at these early times and is expected to perform equally well at later times, it is also true that the spanwise shear stress is relatively small at these early times. The development of the spanwise velocity profile is therefore essentially laminar-like

at these early times and any nonequilibrium model (that starts with small spanwise shear stresses) would also be able to predict the spanwise development at these early times quite well.

Hence, a more stringent test of the turbulent potential was performed by predicting the flow over an infinite swept bump. If sidewall effects and the boundary-layer growth on the top wall are neglected, this flow can be computed as a two-dimensional problem (it is still a three-dimensional boundary layer, however). The flow over a swept bump is an interesting test case because it tests the model's ability to predict a turbulent boundary layer that is subjected to both streamwise pressure gradients and changes in curvature. One more reason for interest in this flow is because of its similarity to the boundary layer over a wing, turbine blades, and so forth. High-quality experimental data are available for this flow as is information about the inlet conditions (Webster et al., 1996). In flows with a single direction of inhomogeneity (such as a flat plate boundary layer) $\phi = R_{22}$ and $\psi_3 = R_{12}$, so the turbulent potentials can be prescribed accurately at the inlet. Wu and Squires (1998) were able to predict three-dimensional boundary layers over a swept bump using the RANS model developed by Durbin (1993b) and using large-eddy simulations.

The bump is defined by three circular arcs (Figs. 5 and 6) and allows the examination of the combined effects of the surface

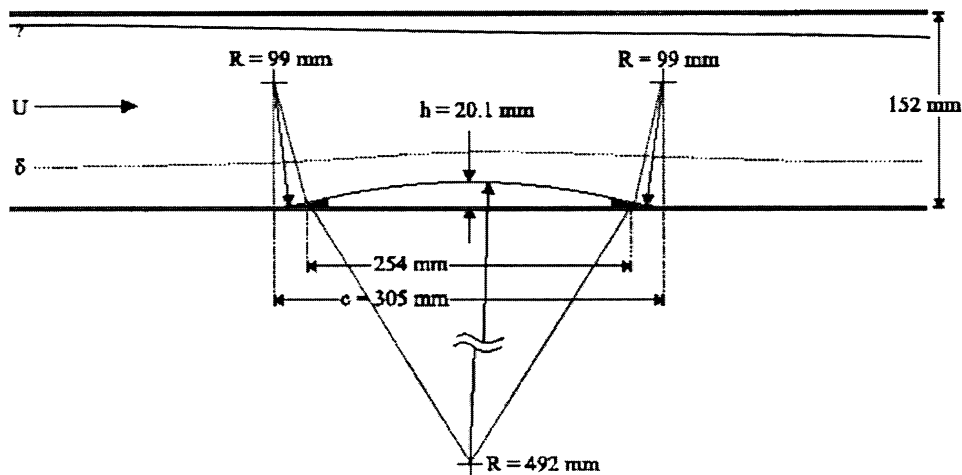


FIGURE 6

Side view of the bump.

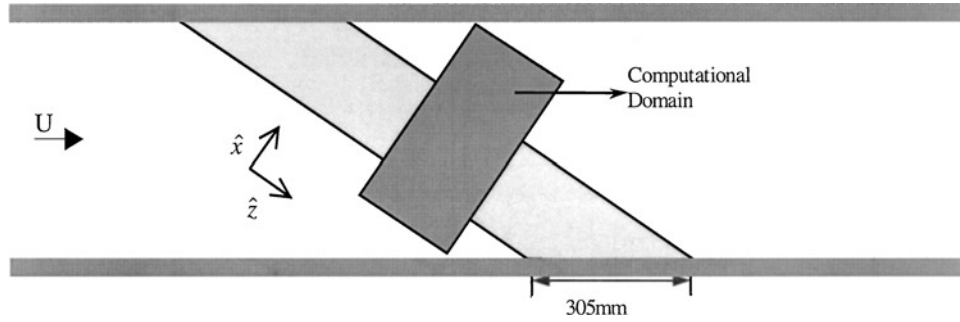


FIGURE 7

Top view of the bump showing the computational domain and the rotated computational coordinate system.

curvature and the streamwise pressure gradients on the mean flow. The boundary layer experiences several changes in the streamwise pressure gradient: at first, mildly adverse, then strongly favorable, strongly adverse and, finally, mildly favorable.

The flow is nearly homogeneous in the direction parallel to the bump because a suction slot is used. If the top boundary layer and the channel sidewall effects are neglected, then a two-dimensional domain (Fig. 7) can be used to calculate the flow. This reference frame will be referred to as the computational frame of reference. It is at an angle of 45 degrees to the original (experimental) frame of reference. An unstructured grid, shown in Figure 8, that has high near-wall resolution is used to calculate the flow.

The inlet condition is $\tilde{W} = U \sin 45^\circ$; $\tilde{U} = U \cos 45^\circ$; and $\tilde{V} = 0.0$. The results are presented in the original wind tunnel reference frame (see Figure 5). Two different cases were simulated: one had an inlet condition of a fully developed, zero-pressure-gradient, two-dimensional boundary layer at $Re_\theta = 1400$; the other had an inlet boundary layer at $Re_\theta = 3260$. The upstream conditions were introduced at a half-bump chord length upstream of the leading edge of the bump. A slip-boundary condition is applied at the top wall. To account for the upper boundary layer growth, the top wall slope is set to roughly match the experimental mass flux. The upper wall is therefore modified by our best estimate of the displacement thickness.

The streamwise velocity profiles for an initial $Re_\theta = 1400$ are shown as a function of the distance from the channel floor y in Figure 9a. U_0 is the initial boundary layer free-stream velocity and distances are given in meters. The results are shown at various positions downstream of leading edge of the bump. The model predictions are the symbols and the experimental results are the lines. The model predictions are in good agreement with the experimental results. The streamwise component of velocity increases and reaches a maximum value at the apex of the bump. On the trailing edge, the flow is very close to separation because of the adverse pressure gradient caused by the flow expansion. The flow relaxes to a two-dimensional boundary layer as it moves downstream of the bump.

The spanwise velocity profiles are shown in Figure 9b. The model predictions are given by symbols and the experimental results are given by lines. The model predictions are in good agreement with the experimental results. The amount of cross flow gives an idea of three-dimensionality of the flow. At the top of the bump the mean flow angle, defined as $\tan^{-1}(w/u)$, is negative and it becomes positive at the rear of the bump. The spanwise component of the velocity, which is negative on top of the bump, increases and reaches a maximum value at the exit of the bump. This change in the sign of the spanwise velocity occurs because the spanwise pressure gradient switches sign once it reaches the top of the bump.

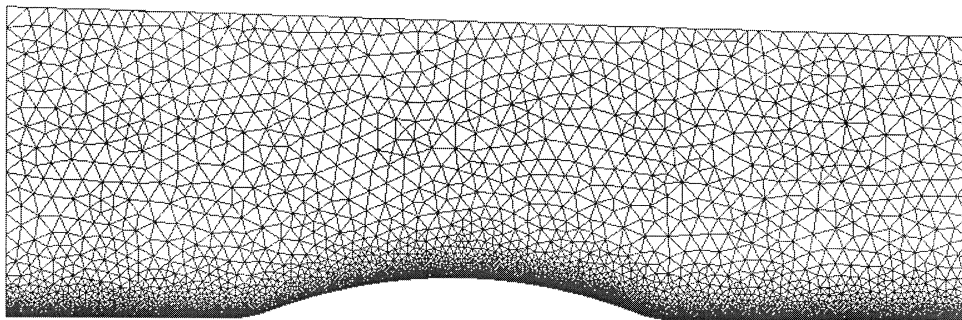
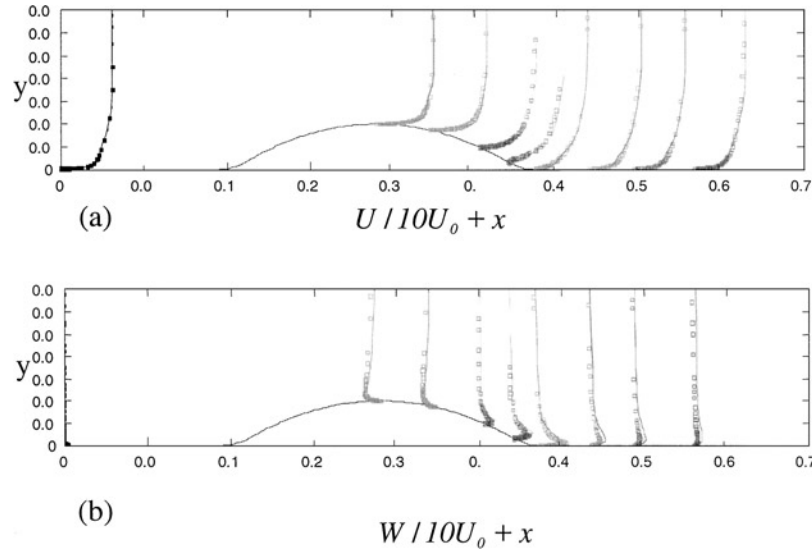


FIGURE 8

Mesh for the swept bump computational domain.

**FIGURE 9**

Velocity profiles in the experimental frame of reference for inlet $Re_\theta = 1400$. The symbols are the model predictions and the lines are the experimental data. (a) Streamwise velocity; (b) spanwise velocity.

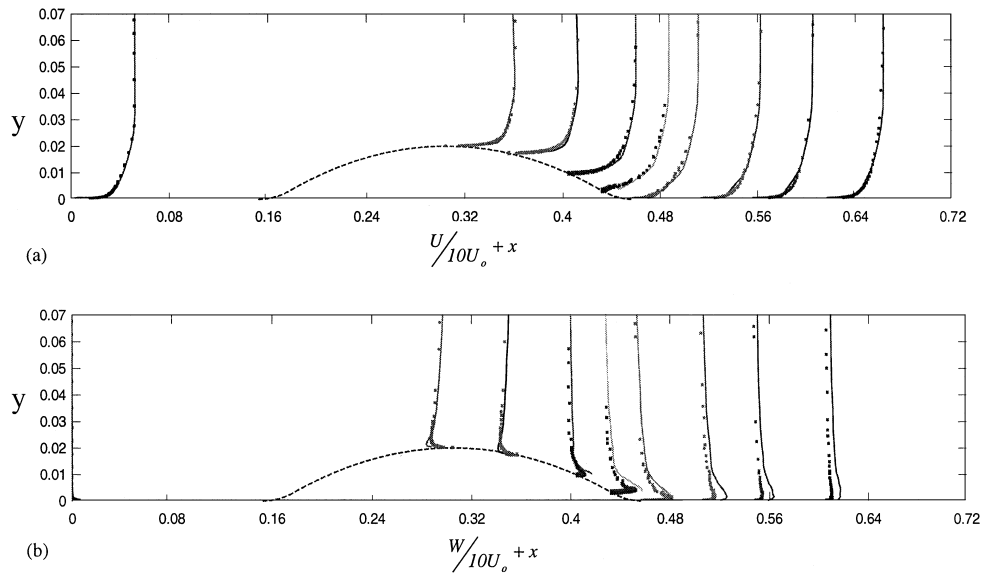
Downstream of the bump, the model seems to recover too quickly compared to the experiment. It is unclear how much of this recovery difficulty is due to the unknown upper boundary layer and sidewall effects, and how much is due to the model. This is the opposite of the recovery problem after a backward-facing step in which the model solution does not recover quickly enough.

Similar results were observed when a zero pressure gradient, two-dimensional boundary layer with $Re_\theta = 3260$ was used as

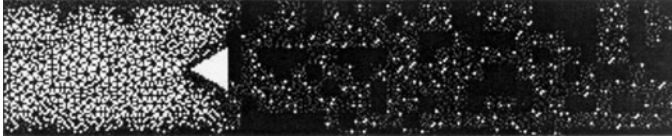
the upstream condition. The streamwise and spanwise velocity profiles scaled using the initial boundary layer edge velocity U_0 for an initial $Re_\theta = 3260$ are shown as the function of the distance from the channel floor y in Figure 10.

UNSTEADY VORTEX SHEDDING

To test this model's ability to predict unsteady nonequilibrium turbulent flow, the problem of vortex shedding behind a two-dimensional triangular cylinder was chosen. The flow is

**FIGURE 10**

Velocity profiles in the experimental frame of reference for inlet $Re_\theta = 3260$. The symbols are the model predictions and the lines are the experimental data. (a) Streamwise velocity; (b) spanwise velocity.

**FIGURE 11**

Computational domain and mesh for flow past a triangular cylinder.

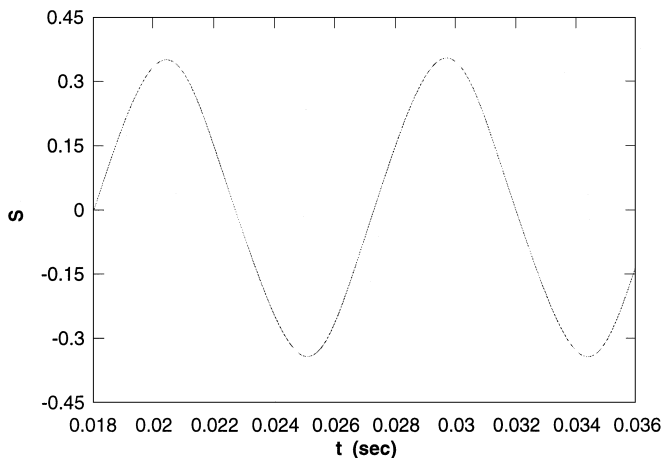
inherently unsteady. Complicated phenomena such as separation and large-scale vortices coexist with the turbulence. This geometry is slightly easier to simulate than the circular cylinder because the separation points are fixed.

The computational domain is shown in Figure 11. It is the same as Sjunnesson's (1991) experiment. Approximately 25,000 triangles are used in this simulation. The inlet mean streamwise velocity is set to a constant and the vertical velocity is set to zero. For turbulent kinetic energy and dissipation rate, we use the same boundary conditions described by Johnnasson (1993).

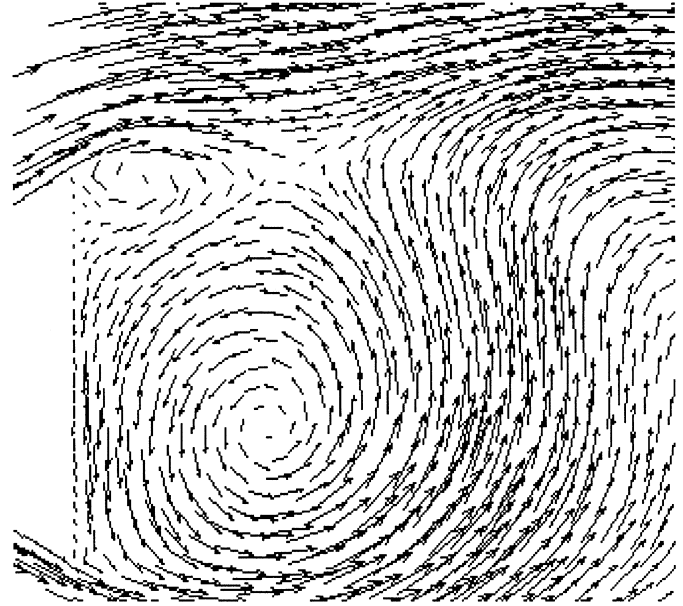
$$U_{in} = 17.0 \text{ m/s}; \quad k_{in} = (0.05U_{in})^2; \quad \varepsilon_{in} = \frac{0.16k_{in}^{3/2}}{0.2\ell}$$

The total mass flow was $\dot{m}_1 = 0.6 \text{ kg s}^{-1}$ in their experiment, and the inlet velocity is evaluated based on that value. These values are also used as the initial value for the whole domain. ℓ is the height of the duct (which is three times the height of the triangle). A zero gradient boundary condition is used for all the variables at the outlet. Slip-wall boundary conditions are used for the duct wall. The Reynolds number of this simulation is $Re = U_{in}d/\nu = 45,000$, where d is the side length of the triangle.

The unsteady behavior was caused by vortices alternately shedding from the upper and lower edges of the cylinder, forming a Von Karman vortex street behind the triangle. No special triggering measure was taken to start the vortex shedding; the un-

**FIGURE 12**

The stream function of one point about one cylinder height behind the triangle near the centerline.

**FIGURE 13**

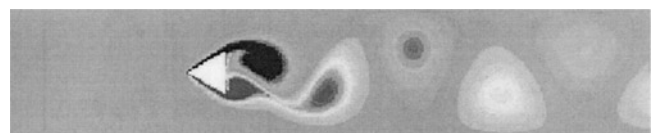
Instantaneous velocity vectors.

steadiness in the computational results evolved naturally. It was triggered by machine error and by the asymmetry of the mesh.

To illustrate the periodicity of the flow, the stream-function of a point about one triangle height behind the triangle near the centerline is shown in Figure 12. It can be seen that an almost perfect periodicity exists. The shedding frequency is $109.3 \text{ (s}^{-1}\text{)}$. The corresponding Strouhal number defined by $Sr = fd/U_{in}$ is 0.257, which should be compared with experimental data of 0.25 and the computed value of 0.27 in Johnnasson (1993). Figure 13 shows an instantaneous velocity vector plot; we can see that the center of a vortex is rolled up at the lower edge and a new vortex is beginning to roll up at the upper edge. The vortex street can also be seen in the instantaneous vorticity contours plot shown in Figure 14.

Although the instantaneous flow is asymmetrical, the time-averaged fields are always symmetrical or antisymmetrical. Figure 15 shows the mean streamwise velocity at the centerline. The length of the recirculation zone is accurately predicted, whereas the location of the maximum negative velocity is slightly upstream compared with the experiments. The magnitude of the maximum negative velocity is also a little lower than indicated by the experiment data.

Figure 16 shows the streamwise velocity at different cross sections behind the triangle. The calculated velocity profiles are

**FIGURE 14**

Instantaneous vorticity contours.

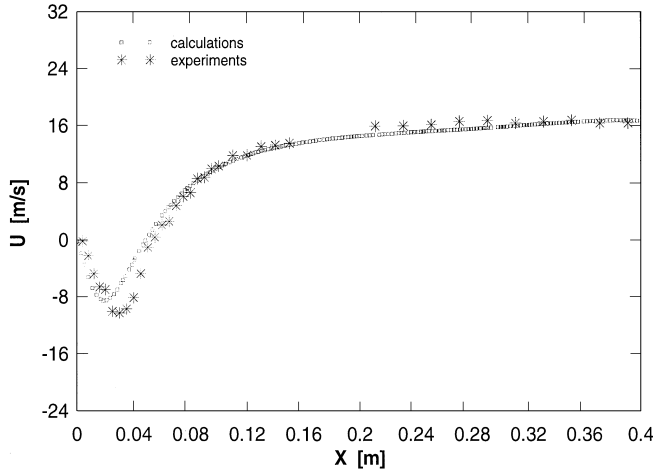


FIGURE 15
Mean streamwise velocity at the centerline.

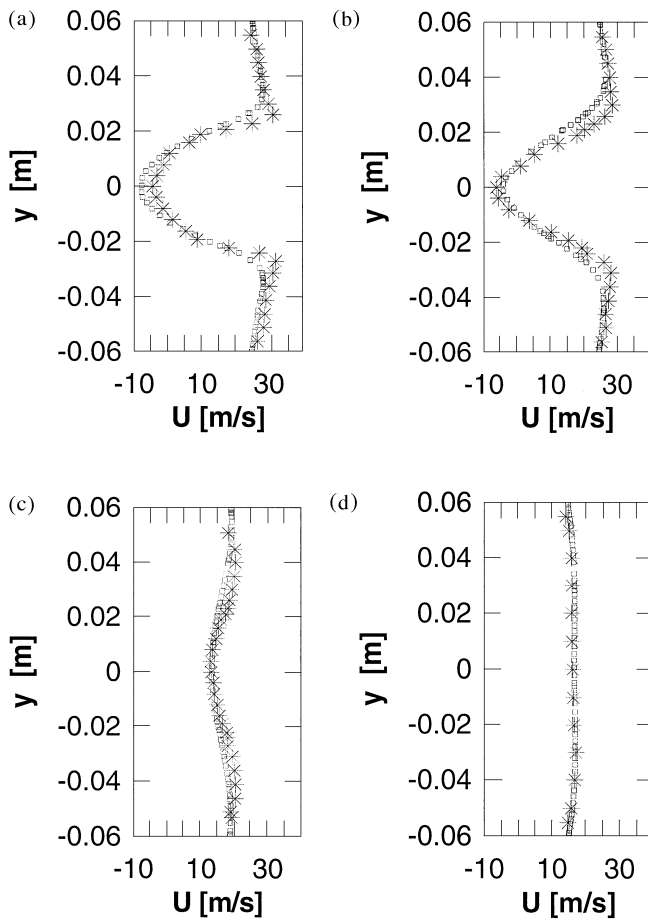


FIGURE 16
Mean streamwise velocity behind the triangle. \square , calculations; *, experiments. (a) 15 mm. (b) 38 mm. (c) 150 mm. (d) 376 mm.

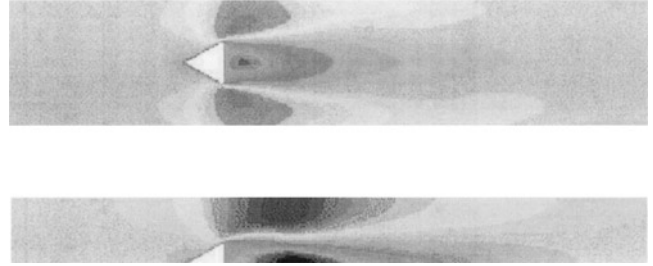


FIGURE 17
Mean streamwise velocity contours of the time-averaged unsteady and steady solution.

in reasonable agreement with the experimental data. However, it is hypothesized that the boundary layer on the triangle is not fully resolved due to mesh-size restrictions. The computed boundary layer is thicker than the real one; thus, close to the back of the triangle, the fluid is slowed down and driven backwards more than it should be. This would explain the mean velocity profile close to the centerline at $x = 15$ mm where the velocity is underpredicted.

In another simulation, we used half of the domain mentioned above and imposed a symmetrical boundary condition along the centerline. Figure 17 shows the comparison of the mean streamwise velocity contours. The top simulation is the time-averaged unsteady streamwise velocity. The bottom simulation is the steady solution imposed by forcing a symmetry condition at the centerline. The contour levels in each plot are the same. The steady solution has a recirculation zone that is much longer than the time-averaged unsteady solution. The reason for this is that the unsteady flow increases the momentum exchange between the wake and its surroundings, thus reducing the recirculation zone. In the steady simulation, the turbulence model does a poor job representing the momentum exchange due to the large shedding vortices.

In this work, a flow past a square cylinder at $Re = 21,400$ (which is based on upstream velocity and cylinder side height d) is also simulated. The geometry and mesh of this simulation is shown in Figure 18. On the left boundary, the x -component

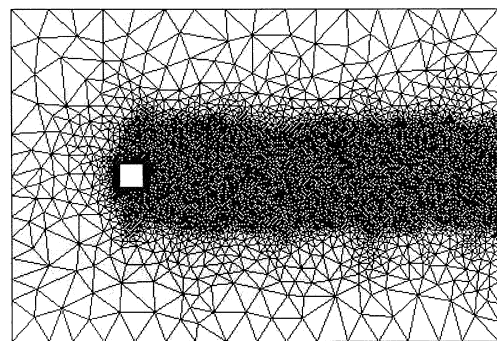


FIGURE 18
Computational domain and mesh for flow past a square cylinder.

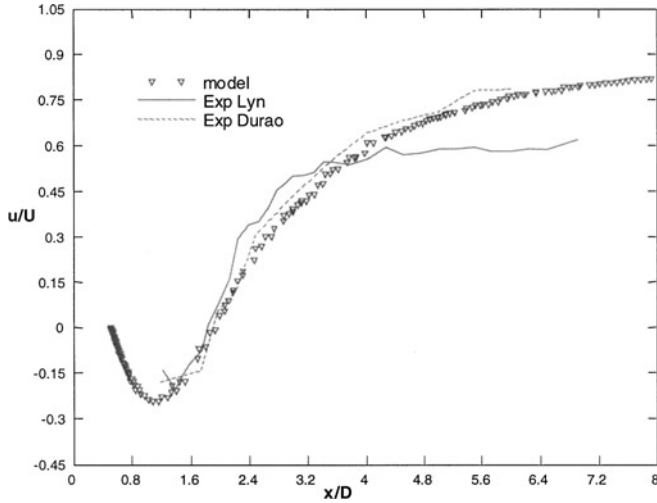


FIGURE 19

The mean streamwise velocity at the centerline for flow over a square cylinder.

velocity is set to a constant while the y -component is set to zero. On the right boundary, dynamic pressure is a constant and the gradient of the y component velocity is zero. The top and bottom boundaries are slip walls. The boundary on the cylinder is a solid wall. The turbulence fluctuation velocity is about 1% of the mean velocity. The turbulence quantities evaluated based on this are taken to be the initial condition and are also fixed on the left boundary (taken as a boundary condition).

Figure 19 shows the mean streamwise velocity at the centerline. Two experimental data sets are available: the data of Lyn and colleagues (1995) and Durao and colleagues (1988) are quite different in the downstream region ($x/d > 4$). When $x/d < 4$, our simulation matches both experiments well. When $x/d > 4$, our simulation is closer to the data of Durao and colleagues. Sim-

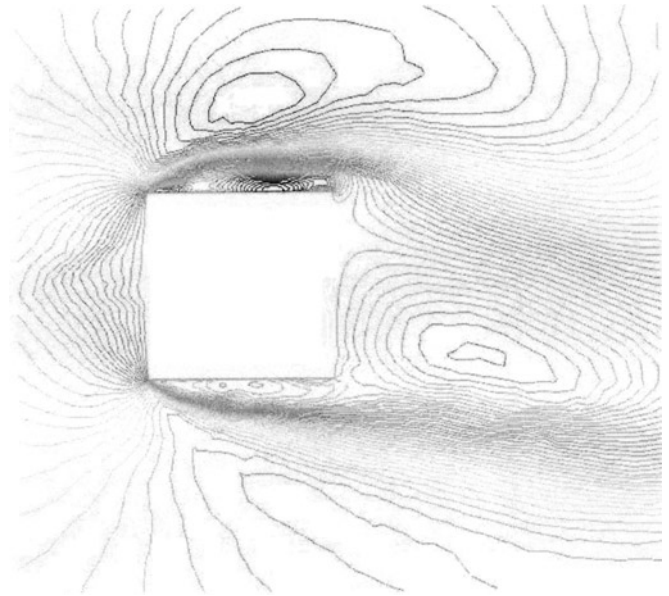


FIGURE 21

Instantaneous x -component velocity contours.

ilar large eddy simulation (LES) results have been reported by Bouris and Bergeles (1996) and Murakami and Mochida (1995).

The time-averaged streamwise velocity is shown in Figure 20 at three downstream cross sections. The calculated predictions are compared with the experiments of Lyn and colleagues (1995). The experimental data in the last cross section shows almost linear behavior near the centerline and no wake development from the previous cross section. This may also explain some of the discrepancy that this data set displays in the previous figure. The first two cross sections are in relatively good agreement with the experimental data.

Figure 21 is an instantaneous streamwise velocity contours plot. As shown in this figure, separation occurs on the top and

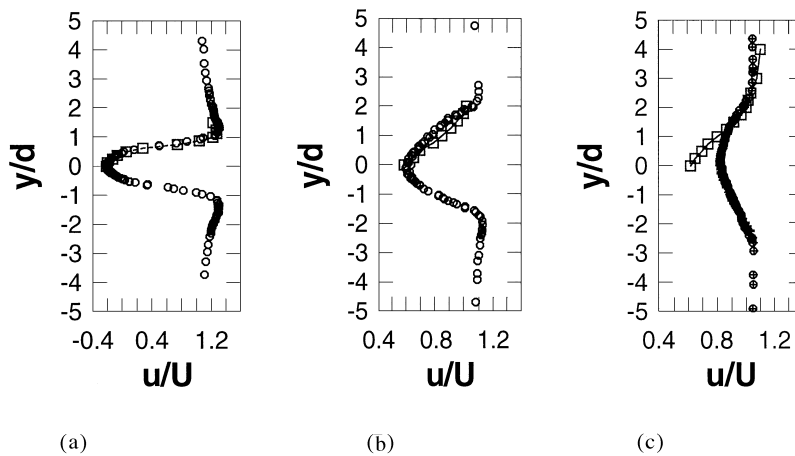


FIGURE 20

Mean streamwise velocity behind the triangle. \circ , calculations; \boxtimes , experiments. (a) $x/d = 1$. (b) $x/d = 3$. (c) $x/d = 6$ downstream of the center of the square.

bottom wall of the square cylinder. The flow pattern of this geometry is more complicated than that of the triangular cylinder where separation occurs on the back corner.

CONCLUSIONS

The turbulent potential model demonstrates the ability to accurately predict the mean flow behavior of the suddenly spanwise-driven channel flow. The effects observed in this flow cannot be reproduced by most RANS models. The turbulent potential model was able to reproduce the observed effects in the turbulence quantities by a small addition to the ε equation. The change in the ε equation is similar to the suggestion proposed by Durbin (1993a). The turbulence quantities show a reasonable agreement with the DNS data and the correct qualitative trends both spatially and temporally. The predictions of the turbulent potential model for the three-dimensional boundary layer over a swept bump are in good agreement with the experimental data for the mean streamwise and spanwise velocity. Given the uncertainties of the experiment (i.e., the top boundary layer and sidewall effects), we can not expect the model predictions to compare any more favorably.

In predicting unsteady vortex shedding, the turbulent potential model shows good overall agreement with the experiments. The shedding frequency is within 5% and the mean flow cross-section and centerline predictions are within the experimental error. Our investigations showed that the model naturally models the turbulence and not the large-scale vortices. The shedding occurs spontaneously in the simulations.

This work has demonstrated the efficacy of the turbulent potential modeling approach for complex nonequilibrium flows. The model accurately predicted both three-dimensional boundary layers and unsteady vortex shedding. Its capability of capturing nonequilibrium turbulent flows and the inexpensive computing cost make the turbulent potential model an attractive approach for engineering applications.

REFERENCES

- Bouris, D., and Bergeles, G. 1996. 2D LES of vortex shedding from a square cylinder. *Journal of Wind Engineering and Industrial Aerodynamics* 80:31–46.
- Bradshaw, P., Launder, B. E., and Lumley, J. L. 1996. Collaborative testing of turbulence models. *Journal of Fluid Engineering* 118:243–247.
- Ölçmen, M. S., and Simpson, R. L. 1993. Evaluation of algebraic eddy-viscosity models in three-dimensional turbulent boundary layers. *AIAA Journal* 31:1545–1554.
- Durao, D. F. G., Heitor, M. V., and Pereira, J. C. F. 1988. Measurements of turbulent and periodic flows around a square cross section cylinder. *Experiments in Fluids* 6:298–304.
- Durbin, P. A. 1993a. On modeling three-dimensional turbulent wall layers. *Phys Fluids A* 5:1231–1238.
- Durbin, P. A. 1993b. A Reynolds stress model for near-wall turbulence. *Journal of Fluid Mechanics* 249:465.
- Durbin, P. A. 1994. Turbulence modeling for separated flow. *Annual Research Briefs*. Stanford, CA: Center for Turbulence Research, Stanford University.
- Fannelop, T. K., and Krogstad, P. A. 1975. Three-dimensional turbulent boundary layers in external flows: a report on Euromech60. *Journal of Fluid Mechanics* 71:815–826.
- Franke, R., and Rodi, W. 1991. Calculation of vortex shedding past a square cylinder with various turbulence models. *Proceedings of the 8th Symposium on Turbulent Shear Flows*, 20.1.1–20.1.6. Munich, Germany: Springer Verlag.
- Johansson, S. H., Davidson, L., and Olsson, E. 1993. Numerical simulation of vortex shedding past triangular cylinders at high Reynolds number using a κ - ε turbulence model. *International Journal for Numerical Methods in Fluids* 16:859–878.
- Lyn, D. A., Einav, S., Rodi, W., and Park, J. H. 1995. A laser-Doppler velocimetry study of ensemble-averaged characteristics of the turbulent near wake of a square cylinder. *Journal of Fluid Mechanics* 304:285–319.
- Moin, P., Shih, T.-H., Driver, D., and Mansour, N. 1990. Direct numerical simulation of three-dimensional turbulent boundary layer. *Phys Fluids A* 2:1846–1853.
- Murakami, S., and Mochida, A. 1995. On turbulent vortex shedding flow past 2D square cylinder predicted by CFD. *Journal of Wind Engineering and Industrial Aerodynamics* 54/55:191–211.
- Perot, J. B. 1999. Turbulence Modeling Using Body Force Potentials. *Physics of Fluids* 11:2645–2656.
- Perot, J. B. 2000. Conservation Properties of Unstructured Staggered Mesh Schemes. *Journal of Computational Physics* 159:58–89.
- Perot, J. B., and Wang, H. 1999. Modeling separation and reattachment using the turbulent potential model. *Proceedings of the 4th International Symposium on Engineering Turbulence Modeling and Measurements*. Corsica, France: Elsevier.
- Perot, J. B., and Zhang, X. 1999. Reformulation of the unstructured staggered mesh method as a classic finite volume method. *Proceedings of the 2nd International Symposium on Finite Volumes for Complex Applications: Problems and Perspectives*, 263–270. Duisberg, Germany: Hermes.
- Sjunnesson, A., Nelsons, C., and Max, E. 1991. LDA measurement of velocities and turbulence in a bluff body stabilized flame. *Volvo Flygmotor AB, Trollhattan, Volvo Report*.
- Webster, R., DeGraff, D. B., and Eaton, J. K. 1996. Turbulence characteristics of a boundary layer over a swept bump. *Journal of Fluid Mechanics* 323:1–22.
- Wu, X., and Squires, K. D. 1998. Prediction of the three-dimensional boundary layer over a swept bump. *AIAA Journal* 36:505–514.



Hindawi

Submit your manuscripts at
<http://www.hindawi.com>

